Research Article | Vol. 31, No. 26 / 18 Dec 2023 / Optics Express 44224
Optics EXPRESS

Multipath artifacts enable angular contrast in multimodal endoscopic optical coherence tomography

A. TANSKANEN,[1,2,5,†] J. MALONE,[1,2,†] C. MACAULAY,[1,3] AND P. LANE[1,2,4,6]

[1]Department of Integrative Oncology, British Columbia Cancer Research Institute, 675 W 10th Ave., Vancouver, BC V5Z 1L3, Canada
[2]School of Biomedical Engineering, University of British Columbia, 251-2222 Health Sciences Mall, Vancouver, BC V6 T 1Z3, Canada
[3]Department of Pathology and Laboratory Medicine, University of British Columbia and Vancouver General Hospital, G227- 2211 Wesbrook Mall, Vancouver, BC V6 T 1Z7, Canada
[4]School of Engineering Science, Simon Fraser University, 8888 University Drive, Burnaby BC V5A 1S6, Canada
[5]atanskanen@bccrc.ca
[6]plane@bccrc.ca
[†]These authors contributed equally to this work

Abstract: Multipath artifacts are inherent to double-clad fiber based optical coherence tomography (OCT), appearing as ghost images blurred in the A-line direction. They result from the excitation of higher-order inner-cladding modes in the OCT sample arm which cross-couple into the fundamental mode at discontinuities and thus are detected in single-mode fiber-based interferometers. Historically, multipath artifacts have been regarded as a drawback in single fiber endoscopic multimodal OCT systems as they degrade OCT quality. In this work, we reveal that multipath artifacts can be projected into high-quality two-dimensional *en face* images which encode high angle backscattering features. Using a combination of experiment and simulation, we characterize the coupling of Mie-range scatterers into the fundamental image (LP_{01} mode) and higher-order image (multipath artifact). This is validated experimentally through imaging of microspheres with an endoscopic multimodal OCT system. The angular dependence of the fundamental image and higher order image generated by the multipath artifact lays the basis for multipath contrast, a ratiometric measurement of differential coupling which provides information regarding the angular diversity of a sample. Multipath contrast images can be generated from OCT data where multipath artifacts are present, meaning that a wealth of clinical data can be retrospectively examined.

1. Introduction

Optical endoscopes exploit the near-lossless transmission, narrow imaging cores and flexibility of fiber optics to provide high resolution minimally invasive imaging in small luminal organs deep within the body. Low signal modalities such as contrast-free fluorescence imaging necessitate multi-mode fibers (MMF), which have high collection efficiencies from refractive index profiles (RIPs) with wide diameter and high numerical aperture cores [1,2]. Confocal endomicroscopy makes use of single-mode fibers (SMF) in place of a pinhole to maintain the optical sectioning properties of a free-space system [3]. Time-gated techniques such as optical coherence tomography (OCT) also require SMF to limit modal dispersion as additional modes introduce ghost images which can obscure the true image. Optical fibers with more complex RIPs further enable more elaborate imaging schemes: multimodal imaging consisting of OCT and additional modality makes use of double-clad fiber (DCF) which has a single-mode core for

#504854 https://doi.org/10.1364/OE.504854
Journal © 2023 Received 1 Sep 2023; revised 24 Nov 2023; accepted 29 Nov 2023; published 12 Dec 2023

Optics EXPRESS

OCT, and a multimode inner-cladding for a complimentary technique [4–15]. OCT provides volumetric imaging of subsurface tissue morphology; thus, functional imaging modalities which provide information regarding tissue biochemistry such as autofluorescence imaging (AFI) are often used in concert.

Our lab implements one such system with the goal of detecting cancers *in vivo*: optical coherence tomography and autofluorescence imaging (OCT-AFI) [16,17]. Carcinoma is frequently characterized by a progressive thickening of epithelial tissue and eventual loss of the basement membrane. Simultaneously, as cancer cells replicate (increasing in size and density in most tissues) the surrounding extracellular matrix of mostly collagen and elastin is degraded and remodeled [18–20]. OCT-AFI can visualize some of these changes: OCT allows for volumetric assessment of superficial tissue stratification while the structural proteins collagen and elastin fluoresce green under blue excitation [21,22].

Utilizing complex RIP geometries to implement multimodal imaging in a single fiber comes at a cost. For instance, the doped cores of DCF generate additional background fluorescence when compared to a pure-silica MMF core, reducing fluorescence image quality [23]. In the OCT modality, imaging with DCF as opposed to SMF results in time shifted multipath artifacts, ghost images smeared in the A-line direction, that may superimpose the fundamental image (FI) [4,24–26]. This is well visualized in Fig. 1(b), where the multipath artifact is located above the FI. The distance between the true image and any multipath artifacts is linearly related to the length of DCF used in the sample arm. In theory, their impacts could be significantly mitigated by using a long length of DCF (>5 m). In practice, the length of DCF in an imaging catheter is typically constrained to <2 m by mechanical and clinical needs; thus, these impacts are generally mitigated by folding the multipath artifact over the zero-reference delay to prevent superposition of over the FI.

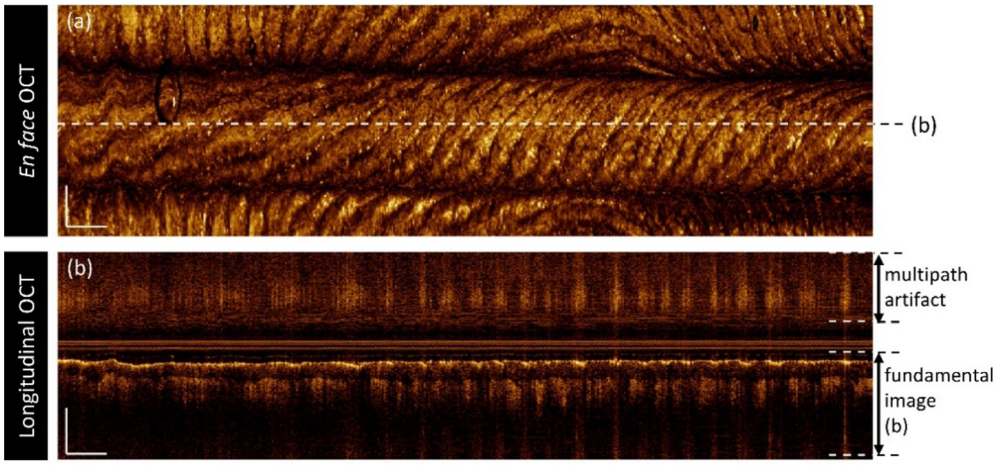

Fig. 1. OCT of human fingertip demonstrating multipath artifacts. Scale bars are 1 mm. The multipath artifacts are present as a hazy, mirrored image which may be separated from the true OCT image in the A-line direction by setting the reference mirror appropriately. (a) *En face* projection of the OCT taken over the region of FI described in (b). (b) Longitudinal cross-section of the OCT taken from the dashed slice in (a).

Previously we have characterized multipath artifacts, correlating their existence to the excitation of core-like inner-cladding modes, which have a prominent LP_{11}-like excitation confined to the geometric area of the presumably single-mode core [27]. Based on this knowledge we demonstrated that a triple-clad W-Type fiber can implement multimodal OCT while preserving single-mode quality imaging [28]. However, in studying multipath artifacts with the goal of

Optics EXPRESS

eliminating them, we noted that features present within the FI (corresponding to the LP_{01} mode) manifested differently within the multipath artifact. Within Fig. 1(b) we observe that light backscattered from the fingertip ridges are more prominently displayed within the FI than the multipath artifact. Inversely, creases appear dark within the FI but bright within the multipath artifact.

Notably, similar phenomena have been deliberately generated in OCT systems which exploit the properties of few-mode fibers (FMF). A 3-mode FMF was used by P. Eugui et al. (2018) in a optical coherence microscopy system to produce three simultaneous views (corresponding to the LP_{01}, LP_{11}, and LP_{21} modes) of cancerous glioblastoma tissue and neuritic plaques [29–31]. The temporal delays of each mode were used to separate the three views within a single OCT tomogram. M. Poinsinet de Sivry-Houle et al. (2021) applied a modally specific photonic lantern to separate the LP_{01} and LP_{11} modes of a FMF into separate interferometers to isolate the signals from each mode [32]. In both applications, the modes of the FMFs sample different angular characteristics of the light backscattering off the tissue specimen: the higher-order modes (HOMs) correspond to light backscattered at higher angles when compared to the fundamental LP_{01} mode. Contrast between this "simultaneous bright and darkfield" effect may allow for interrogation of sub-resolution features such as particle size and density in the Mie scattering regime. From a biological standpoint, FMF-based OCT may be sensitive to the changes in nuclear size and density associated with carcinogenesis.

We hypothesize that the multipath artifacts associated with DCF in multimodal OCT systems produce the same effect, encoding light backscattered at high angles into the core-like inner-cladding modes (multipath artifact) and low angles into the FI. Herein, a combination of simulation and experiment is used to quantify the angular coupling into the image mode (LP01) and the HOMs of the multipath artifact. Finally, we demonstrate how to utilize the contrast between the signal coupled into the fundamental image versus the artifact as an additional imaging modality. To accompany this change in perspective, we re-label the multipath artifact as the higher-order image (HOI), owing to the HOMs responsible for its existence.

2. Theory

Within FMF-based OCT, it is critical to overcome the orthogonality of the modes to ensure the interference between the LP_{01} mode of the reference arm and the HOMs from the sample is non-zero. This has been achieved previously by either laterally offsetting the sample and reference beams, or by using the modally-specific photonic lantern to cross-couple HOMs into the LP_{01} mode of a SMF [31,32]. However, within many multimodal OCT systems, signal coupled into the HOMs is detected *despite no such scheme being implemented*. To understand how this occurs, it is necessary to understand the components of a multimodal OCT system. As an example, we describe the components along the sample arm of our OCT-AFI system.

To merge the two modalities into a single-fiber imaging catheter, a wavelength division multiplexer (WDM) couples the infrared (1310 ± 50 nm) OCT and the blue (450 nm) AFI excitation signals into a SMF with a 1250 nm cut-off wavelength. The WDM output is connected to the SMF input of a double-clad fiber coupler (DCFC), coupling the two beams into the core of a DCF. This is then connected to a DCF fiber optic rotary joint (FORJ), which provides rotary scanning. Along the return path, the DCFC separates the light coupled into the inner-cladding of the DCF endoscope into an AFI subsystem, while the signal coupled into the core is sent to a SMF OCT interferometer. In prior work, we determined that the spatial delays between the FI and HOI increased linearly with the length of the DCF within the catheter [27]. Here, we iterate upon the formulations for FMF-based OCT described by Eugui *et al* [29], and integrate the angular coupling model presented by Sivry-Houle *et al* [32], to demonstrate the mechanism for HOI generation in DCF-based endoscopic OCT systems. The mechanism is demonstrated graphically in Fig. 2.

Optics EXPRESS

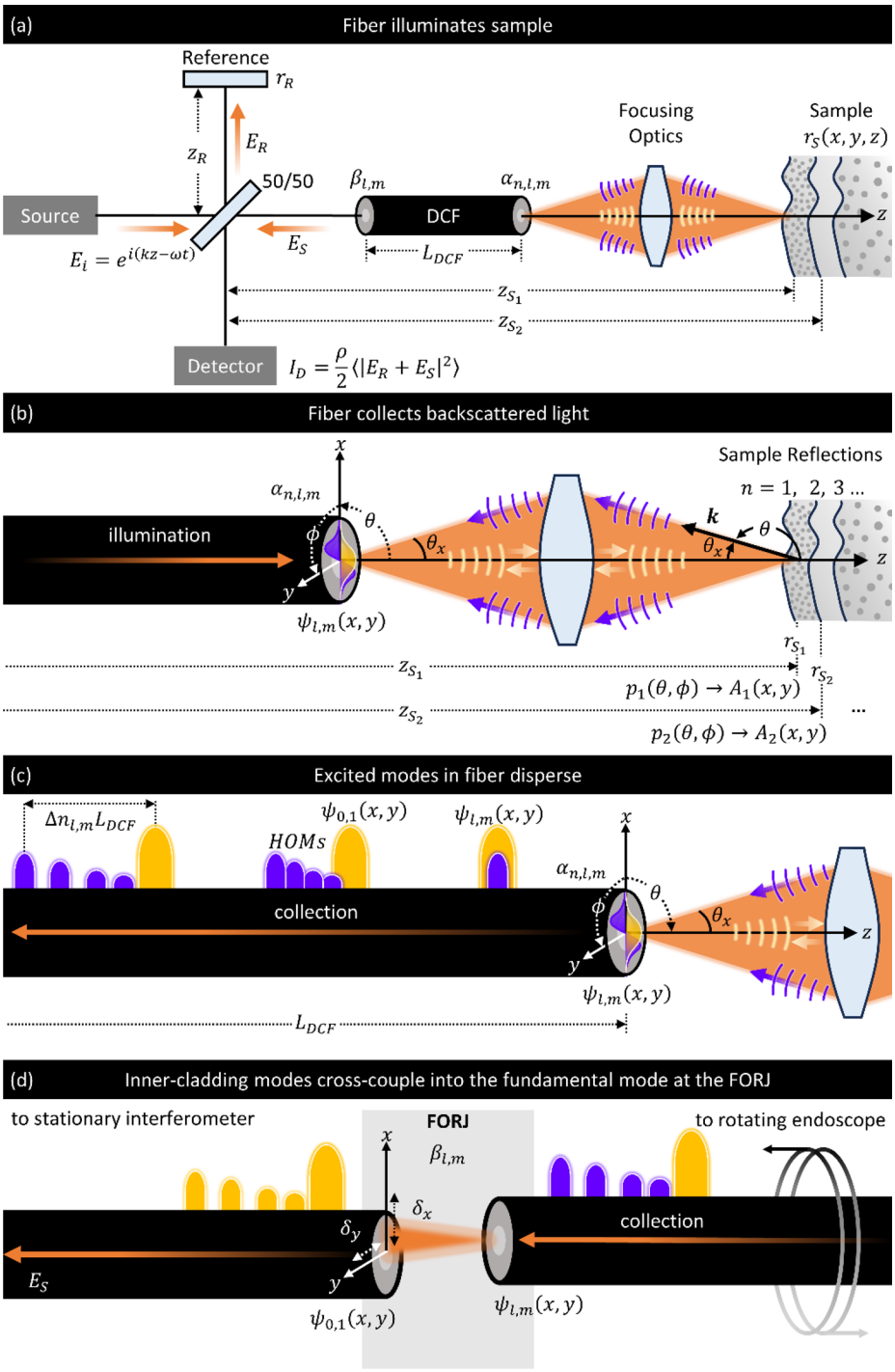

Fig. 2. DCF-based OCT HOI mechanism. The FI signal is denoted in gold, while the HOI signals are denoted in purple. (a) Light incident from an interferometer is focused onto a sample and backscattered onto a DCF. (b) The angular dependent electric field excites both core and inner-cladding modes within the DCF. (c) Inner-cladding modes become temporally displaced as they travel along the length of the fiber, as illustrated by the separation between purple and gold pulses. (d) Small displacements across a fiber joint cause the HOMs to cross-couple into the fundamental mode of the receiving optical fiber.

Optics EXPRESS

Following the nomenclature and framework used by Izatt [33], consider the Michelson interferometer illustrated in Fig. 2(a). The interferometer is illuminated by a polychromatic plane wave with electric field $E_i = s(k,\omega)e^{i(kz-\omega t)}$, where $s(k,\omega)$ is the electric field amplitude as function of wavenumber $k = 2\pi/\lambda$ and angular frequency $\omega = 2\pi\nu$, λ is wavelength, and ν is frequency. For simplicity, distances along the optical axis are measured as if they are in free space, though in practice multimodal DCF systems employ a fiber interferometer. The reference reflector is assumed to have an electric field reflectivity r_R, and power reflectivity $R_R = |r_R|^2$. The reference path is in air and the distance from the beam splitter to the reference reflector is z_R.

The sample under interrogation is characterized by a depth- and angular-dependent reflectivity, $r_S(x,y,z)$. As illustrated in Fig. 2(b), we consider the sample to be composed of a series of N discrete angle-dependent reflections given by $r_S(x,y,z) = \sum_{n=1}^{N} r_{S_n} A_n(x,y)\,\delta(z - z_{S_n})$, with each reflection characterized by its electric field reflectivity $[r_{S_1}, r_{S_2}, \ldots, r_{S_N}]$ or power reflectivity $R_{s_n} = |r_{s_n}|^2$, path length from the beam splitter $[z_{S_1}, z_{S_2}, \ldots, z_{S_N}]$, and a complex envelope $[A_1(x,y), A_2(x,y), \ldots, A_N(x,y)]$ that encodes the angular distribution of the backscattered light. The Fourier transform of the complex envelope $\tilde{A}_n(k_x,k_y)$ describes the angular distribution of the backscattered light, where $k_x = k\theta_x$ and $k_y = k\theta_y$ are angular spatial frequencies along the x- and y-axes under the paraxial approximation, θ_x is the angle between the wavevector and the yz-plane, and θ_y is the angle between wavevector and the xz-plane. When $A_n(x,y) = 1$, then $\tilde{A}_n(k_x,k_y) = \delta(k_x,k_y)$, and the reflected light consists of backscattered light with scattering angle $\theta = \pm 180°$. Similarly, a reflector with isotropic scattering has $A_n(x,y) = \delta(x,y)$ and $\tilde{A}_n(k_x,k_y) = 1$. A reflector that backscatters at an angle $\theta_x < 180°$ to the optical axis will have $A_n(x,y) = e^{ik\theta_x x}$ and $\tilde{A}_n(k_x,k_y) = \delta(k_x - k\theta_x,\ k_y)$. The complex envelope $A_n(x,y)$ corresponding to an arbitrary scattering phase function $p_n(\theta)$ can be determined by first translating the coordinate axis by 180° to bring backscattered light to the origin then taking the Fourier transformation of the resulting phase function.

Illumination light is propagated in the fundamental mode of the DCF (LP_{01} core mode) and projected into the sample by the lens shown in Fig. 2(b). Azimuthally symmetric (ϕ in Fig. 2(b)) light backscattered along the optical axis is coupled into the fundamental mode of the DCF fiber. Light backscattered at a non-zero angle θ to the optical axis may only be partially coupled into the fundamental mode, with some fraction of the power coupled into one or more high-order modes of the DCF. The power fraction coupled into a particular mode depends on its spatial overlap with the incident electric field $A_n(x,y)$. Using an overlap integral, we define the power coupled from discrete reflection n into linearly polarized mode LP_{lm} of the DCF fiber as,

$$\alpha_{n,l,m} = \frac{\left|\iint A_n(x,y)\psi^*_{l,m}(x,y)dxdy\right|^2}{\iint |A_n(x,y)|^2 dxdy \iint |\psi^*_{l,m}(x,y)|^2 dxdy} \tag{1}$$

where $\psi_{l,m}$ is the transverse mode profile of LP_{lm}, l and m are the azimuthal and radial mode orders, and the integration is over the end face of the DCF. Equivalently, the coupling coefficient can also be calculated in the spatial frequency domain,

$$\alpha_{n,l,m} = \frac{\left|\iint \tilde{A}_n(k_x,k_y)\tilde{\psi}^*_{l,m}(k_x,k_y)dk_xdk_y\right|^2}{\iint |\tilde{A}_n(k_x,k_y)|^2 dk_xdk_y \iint |\tilde{\psi}^*_{l,m}(k_x,k_y)|^2 dk_xdk_y} \tag{2}$$

where $\tilde{\psi}_{l,m}(k_x,k_y)$ is the Fourier transform of the transverse mode profile and the integration is over the angles supported by the aperture of the lens.

Ideal backscatter ($\theta = \pm 180°$, $\theta_x = \theta_y = 0$) is coupled almost entirely into the fundamental mode and thus the coupling coefficient as defined above is close to one. Light that is not as

Optics EXPRESS

directly backscattered may partially couple into the fundamental mode and several HOMs as characterized by $\alpha_{n,l,m}$. As we will see, this angle-dependent mode coupling provides a means to differentiate scatterers via scattering angle distribution, and with further analysis, may allow one to elucidate the scattering angle distribution of the light backscattered from a reflector.

As has been described by de Sivry-Houle *et al.*, HOMs with a non-zero azimuthal mode order (e.g. LP_{11} in a step-index fiber) are sensitive to non-orthogonal incident light ($\theta_x, \theta_y > 0$) only if the reflector is displaced some small distance (δ_x, δ_y) from the optical axis [32]. Consequently, if such a reflector is on axis ($\delta_x = \delta_y = 0$), the overlap integral given by Eqs. (1) and (2) is zero. In a scanning system, this means maximum sensitivity to a reflector with angle-dependent backscatter will occur when the reflector is slightly offset from the optical axis. To accommodate for this offset required for sensitivity, de Sivry-Houle *et al.* proposed using the mean coupling coefficient,

$$\tilde{\alpha}_{n,l,m} = \frac{\iint |\tilde{A}_n(k_x, k_y)\tilde{\psi}^*_{l,m}(k_x, k_y)|^2 dk_x dk_y}{\iint |\tilde{A}_n(k_x, k_y)|^2 dk_x dk_y \iint |\tilde{\psi}^*_{l,m}(k_x, k_y)|^2 dk_x dk_y} \tag{3}$$

as a surrogate for the true coupling coefficient defined above. Note the absolute square now operates directly on the Fourier transform of the complex envelope and transverse profile rather than the integral. This is equivalent to integrating over the offset-dependent coupling coefficient $\tilde{\alpha}_{n,l,m}(\delta_x, \delta_y)$ and effectively removes the offset dependency from the coupling coefficients.

An angle-dependent reflection from each discrete reflector is decomposed by the DCF fiber into a set of LP_{lm} modes which propagate down the fiber. Each mode propagates with a unique effective refractive index and phase velocity. HOMs with effective refractive indices less than the fundamental mode will propagate faster (Fig. 2(c)) and appear closer to the zero-reference delay in a processed OCT image, permitting modes which correspond to higher-angle backscatter to be identified given sufficient delay.

The now-dispersed HOMs must be recoupled back into the fundamental mode to interfere with light from the reference reflector (Fig. 2(d)). This typically occurs at fiber joints (e.g., splices, FORJs) where a slight offset exists between the axis of the fibers (δ_x, δ_y). We use the overlap integral,

$$\beta_{l,m} = \frac{\left| \iint \psi_{0,1}(x, y)\, \psi^*_{l,m}(x \pm \delta_x,\ y \pm \delta_y)\, dxdy \right|^2}{\iint |\psi_{0,1}(x, y)|^2 dxdy \iint |\psi^*_{l,m}(x \pm \delta_x,\ y \pm \delta_y)|^2 dxdy} \tag{4}$$

to characterize the power coupling from LP_{lm} to LP_{01}, where the spatial-domain integration is over the end face of the receiving DCF fiber.

Finally, we present the electric fields incident on the beam splitter. That returning from the reference reflector is simply $E_R = \frac{E_i}{\sqrt{2}} r_R e^{i2kz_R}$, while that returning from the sample arm is,

$$E_S = \frac{E_i}{\sqrt{2}} \sum_{n=1}^{N} \sum_{l=0}^{L} \sum_{m=1}^{M} \sqrt{R_{S_n}}\ \sqrt{\alpha_{n,l,m}\, \beta_{l,m}}\ e^{ik(2z_{S_n} + \Delta n_{l,m} L_{DCF})}. \tag{5}$$

The field at the beam splitter is the sum of all modes and all discrete reflectors. The factor of 2 in the first term of the exponential accounts for the round-trip path length to each reflection. The second term, $\Delta n_{l,m} L_{DCF}$, is non-zero for high-order modes, reducing the effective pathlength of the reflection and translating it in the negative z direction. The effective refractive index difference, $\Delta n_{l,m} = n_{l,m} - n_{0,1}$, is definitionally negative for HOMs, where $n_{l,m}$ is the effective refractive index of mode (l, m). The physical length of the DCF fiber L_{DCF}, is multiplied by the mode-dependent refractive-index difference to calculate the phase offset resulting in a translation of the HOM reflection in the negative z. direction.

The detector generates a photocurrent $I_D = \frac{\rho}{2}|E_R + E_S|^2$ proportional to the square of the sums of the reference and sample electric fields, where ρ is the responsivity of the detector,

Optics EXPRESS

and the angled brackets represent time averaging. The spectral interferogram contains DC, cross-correlation, and auto-correlation terms. The cross-correlation terms,

$$I_{OCT}(k) = \frac{\rho}{4} S(k) \left\{ \sum_{n=1}^{N} \sqrt{R_R\, R_{S_n}} \sqrt{\alpha_{n,0,1}\beta_{0,1}} \cos[2k(z_R - z_{S_n})] + \sum_{n=1}^{N} \sum_{l=1}^{L} \sum_{m=1}^{M} \sqrt{R_R\, R_{S_n}} \sqrt{\alpha_{n,l,m}\beta_{l,m}}\, \cos[k(2(z_R - z_{S_n}) + \Delta n_{l,m} L_{DCF})] \right\} \tag{6}$$

encode the position, reflectivity, and angular distribution of the reflectors, where $S(k) = |s(k, \omega)|^2$ is the power sctrum of the source. Note the term owing to the fundamental mode ($l = 0,\ m = 1$) has been written explicitly to distinguish it from the terms responsible for the higher order modes. An inverse Fourier transform can then be applied to recover the A-line profile,

$$i_{OCT}(z) = \frac{\rho}{4} \gamma(z) \otimes \left\{ \sum_{n=1}^{N} \sqrt{R_R\, R_{S_n}} \sqrt{\alpha_{n,0,1}\beta_{0,1}}\ \ \delta[\mathrm{z} \pm 2(z_R - z_{Sn})] + \sum_{n=1}^{N} \sum_{l=1}^{L} \sum_{m=1}^{M} \sqrt{R_R\, R_{S_n}} \sqrt{\alpha_{n,l,m}\beta_{l,m}}\ \delta[\mathrm{z} \pm 2(z_R - z_{Sn}) + \ \Delta n_{l,m} L_{DCF}] \right\} \tag{7}$$

where $\gamma(z)$ is the coherence (or point spread) function, $\otimes$ is the convolution operator, and δ is the Dirac delta function.

Cross-coupling in a DCF FORJ from a HOM in the rotor to the fundamental mode in the stator is highest when there is a large spatial overlap in the geometric area of the core. This holds in our practical experience, where only azimuthal modes of order $l = 1$ are cross-coupled sufficiently (high $\beta_{l,m}$) into the fundamental mode for detection through interference with the Ref. [28]. This results in a HOI which is consistently composed of the same HOMs, and thus will appear in the same location relative to the fundamental mode within a given A-line. Although this equation was derived for a DCF, it is equally applicable to MMF and FMF-based OCT systems which incorporate rotary catheters. However, it differs subtly from the equations derived for the FMF system presented by P. Eugui et al [29]. Here, we have incorporated and described the modal coupling efficiency described by $\alpha_{n,l,m}$ into the OCT cross-correlation equation. Additionally, the FMF system directly interferes the fundamental and HOMs of the sample arm with the fundamental mode of the reference arm. Instead, the HOMs of catheter-based systems are cross-coupled into the fundamental mode of the sample arm (described by $\beta_{l,m}$), which then interferes with the reference fundamental mode.

To leverage the differential coupling into the FI and HOI, we propose the use of multipath contrast (MC). We define MC as the ratio between the powers coupled into the FI versus the HOI, which can be formulated from Eq. (7) as follows:

$$MC = \frac{\sum_{n=1}^{N} \sqrt{R_{S_n}} \sqrt{\alpha_{n,0,1}\beta_{0,1}}}{\sum_{n=1}^{N} \sum_{l=1}^{L} \sum_{m=1}^{M} \sqrt{R_{Sn}} \sqrt{\alpha_{n,l,m}\beta_{l,m}}} \tag{8}$$

The MC is a function of the cross-coupling efficiencies $\beta_{l,m}$ through a discontinuity (the FORJ) and the FI and HOI coupling efficiencies $\alpha_{n,l,m}$. Notably, the ratiometric nature of Eq. (8) removes any dependency on the reflectivity of the reference arm, thus limiting the variance in MC response from changes in the reference arm position or focus. Assuming the modal cross-coupling efficiencies of the FORJ remain constant between images, MC is proportional to the ratio of a backscattered electric field sampled at low angles (by the LP_{01} mode) over the field sampled at higher angles (HOMs of the form LP_{11}-like).

Optics EXPRESS

3. Materials and methods

3.1. Spatially and spectrally resolved imaging through a rotary joint

We seek to determine whether the differential coupling of backscattered light into the FI and HOI can be leveraged to gain additional insight into a sample. Previously, we determined that the HOI corresponded to LP_{11}-like modes [27]. Now, we expand this analysis by characterizing the cross-coupling efficiency of the FORJ (quantifying $\beta_{l,m}$) in our OCT-AFI system and determining the specific modes excited during imaging that comprise the HOI.

For this experiment, the spatially and spectrally (S^2) resolved imaging method was applied using a DCF FORJ to excite modes within a 50 cm length of DCF (Fig. 3) [34,35]. A custom tunable wavelength source scans 560 wavelengths between 1266-1357 nm linearly spaced in wavenumber. Images of the end-face of the fiber are acquired for each wavelength using an InGaAs infrared camera (Ninox 640 II: 640×480-pixel array, 15×15 µm pixel pitch, Raptor Photonics, Milbrook, Northern Ireland). The result is a series of images showing the changes in transmission through the DCF as a function of wavelength. This can then be mapped into a function of the changes in effective refractive index $\Delta n_{l,m}$ (or equivalently, time delay) relative to the fundamental mode through a Fourier transform of the wavenumber data. Encoded within the Fourier transformed data will be the transverse mode profiles (TMP) of each mode excited at their respective effective refractive index ($560 \times 640 \times 480$ image volume). The prominent excitations are identified by calculating the maximum value achieved for each 640×480 image and plotting the results as a function of effective refractive index. Prominent peaks within these plots will correspond to excited modes. The wavelength dependence of the effective refractive index is then examined with by taking a continuous short-wave Fourier transform of the intensity fluctuations of each pixel (here a Stockwell transform is used) to produce a spectrogram [36,37].

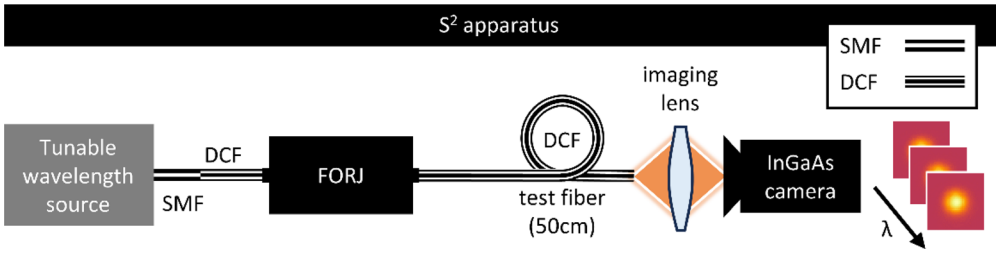

Fig. 3. Experimental apparatus for the S^2 imaging method. A FORJ is used to excite modes within a piece of DCF test fiber; images are taken using an InGaAs camera linearly spaced in wavenumber over a given wavelength band.

To elucidate specific modes corresponding to TMPs resolved within the geometric area of the cladding, we compare the range of $\Delta n_{l,m}$ values corresponding to the LP_{11}-like modes responsible for the HOI to candidate inner-cladding modes generated using a simulation software (RP Fiber Pro). The simulated DCF RIP used to generate these modes has been detailed in our previous work [28]. All potential modes which could be excited at the center wavelength of our OCT system (1310 nm) are generated. Candidate first order azimuthal modes (of the form LP_1 m), which have a $\Delta n_{l,m}$ value within the range of values corresponding to the broad excitation of the HOI can then be identified.

3.2. Differential coupling of Mie scatterers

From their TMPs, we anticipate that some angular scattering distributions will couple preferentially into the FI or HOI. With the candidate HOMs excited across the FORJ identified in experiment 3.1, we can quantify the coupling efficiency of scatterers into the HOI. This can then be compared

Optics EXPRESS

to the coupling of scatterers into the FI to quantify the differential coupling, or MC. Mie scatterers with a range of diameters will be modelled to explore the relationship between MC and scatterer size.

The FI TMP is chosen as the mode excited at $\Delta n_{l,m} = 0$ and the HOI TMPs are chosen for values of $\Delta n_{l,m}$ over the expected region of excitation (previously characterized, [27]). We model the mean coupling efficiency of a beam scanned across a sample using Eq. (3). For this, it is necessary that the TMPs and the scattering phase functions of the sample field both be far-field (Fourier space) representations. Thus, we Fourier transform each of the TMPs measured using the S2 method to construct their angular representation and determine the average coupling into these modes for the backscattered light from different sized polystyrene spheres immersed in water.

The scattering phase functions for microspheres with diameters between 2-20 μm over a wavelength range of 1260-1360 nm are calculated using MatScat, an open-source MATLAB package [38–40]. This range of sphere sizes is selected to be above the upper limit of Rayleigh scattering at 1310 nm, but sub-resolution to our catheter's focusing optics (~26.5 μm in water). Moreover, these sizes are within the expected range of epithelial/cancerous cell nuclear sizes for tissues of interest (lung, oral cavity, cervix) [41–43]. Following, Eq. (8) can be used to calculate the expected MC of each sphere diameter, averaged over all the simulated wavelengths (1260–1360 nm).

3.3. Differential coupling in endoscopic OCT-AFI

To validate the expected coupling of Mie scatterers into the FI and HOI from section 3.2, we image microspheres of different sizes using a previously described endoscopic OCT-AFI system (Fig. 4) [16]. The OCT subsystem uses a 1310 ± 50 nm swept source laser (SSOCT-1310, Axsun Technologies Inc., Billerica, MA, USA) with an SMF Mach-Zehnder interferometer (MZI) and a balanced photodetector (BPD, PDB420C, Thorlabs, Newton, New Jersey, USA). The AFI subsystem uses a 450 nm (LP450-SF15, Thorlabs) blue laser as an excitation source. The output from each subsystem is combined using a wavelength division multiplexer (WD6513A, Thorlabs) and coupled into the core of a DCF (SM-9/105/125-20A, Nufern, USA) connected to a DCF fiber optic rotary joint (FORJ, Princetel, Hamilton Township, New Jersey, USA). A custom rotary pullback drive allows for in-house fabricated DCF image catheters to be actuated in a helical scan pattern. On the return path, autofluorescence is collected within the inner-cladding of the DCF and separated from infrared OCT signal coupled into the core using a double-clad fiber coupler (DCFC, DC1300LEFA, Thorlabs). The DCFC separates the core modes and couples them back into the SMF MZI, while inner-cladding modes are passed into a photo-multiplier tube (PMT, H9433-201, Hamamatsu, Japan) with a long-pass wavelength filter (E480LPXT, Chroma, Bellows Falls, VT, USA) for AFI. The image catheter design makes use of DCF, MMF, no-core fiber, and gradient index fiber for the focusing optics. The catheters used have a measured beam waist of 35 μm in air, or 26.5 μm in water. The OCT subsystem utilizes only SMF. MMF is used to pass the low-signal AFI into the PMT in the AFI subsystem.

We image two separate dilutions (10,000 ppm in water) of sub-resolution polystyrene spheres with diameters of 10 and 15 μm (FluoSpheres F8830 and F8838, ex/em: 430/465 nm, Invitrogen). The catheter tip was inserted into each dilution and OCT was acquired with a 1 mm/s pullback rate and a total of 3008 A-lines per frame. From each tomogram, the FI and HOI resulting from 15 individual microspheres were manually segmented and averaged together into a single point spread function for each sphere size. The total power coupled into the FI and HOI is calculated by summing the intensity of the pixels above background over the area occupied by each signal. The MC is then calculated by dividing the total power of the FI by the HOI. Results from this experiment are compared to the differential coupling model developed in section 3.2.

Optics EXPRESS

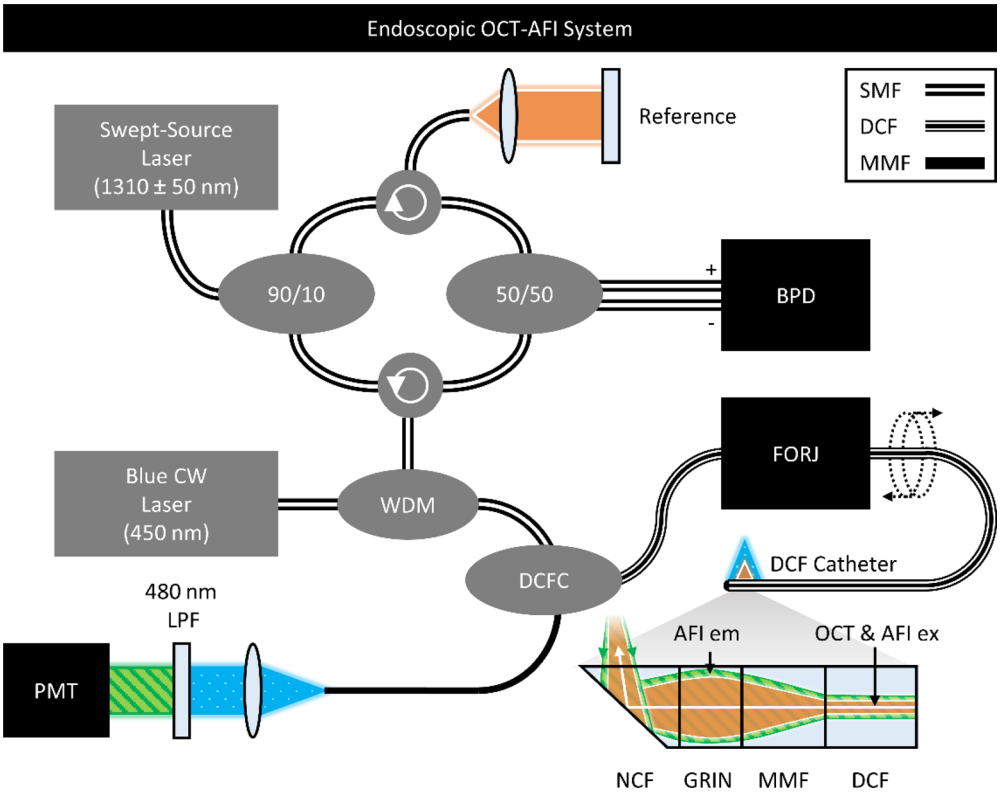

Fig. 4. The endoscopic OCT-AFI system. A swept source laser centered at 1310 nm and a fiber-based Mach-Zehnder interferometer allow for OCT. Signal is collected with a balanced photodetector (BPD). AFI is coupled into this system through a wavelength division multiplexer (WDM) and double clad fiber coupler (DCFC), such that blue excitation light from the 450 nm CW laser is coupled into the core of the image catheter. Emitted light is collected in the cladding, a long pass filter (LPF) is used to remove any reflected blue light before the signal is collected by a photomultiplier tube (PMT). The focusing optics consist of spliced DCF, MMF, gradient index fiber (GRIN), and no-core fiber (NCF), used to focus and deflect the beam.

Optics EXPRESS

3.4. In vivo multipath contrast imaging

We perform retrospective image analysis on two *in vivo* images acquired with the OCT-AFI system described above to assess whether the HOI and FI capture unique information from a biological specimen. This also serves to assess whether this technique is stable in a clinical environment.

In our application, the blurring of the HOIs in the OCT A-line direction (Fig. 1(b)) greatly obscures the information they encode. In this regard, HOIs remain deleterious to imaging in three-dimensions; however, a simple projection in the A-line direction will produce a high-quality two-dimensional image. We can further demonstrate that these projections are different representations of the same sample by taking the pixel-wise division of the *en face* FI over the HOI. We denote this as a *multipath contrast image* (MCI), analogous to the MC described above: a ratiometric representation of the total power coupling in the FI versus HOI.

First, we demonstrate MCI of the human fingertip previously shown in Fig. 1. This is a well-understood OCT phantom that allows for the visualization of tissue layers when viewed as a cross-section, and demonstrates surface features (ridges, fingerprint) which we anticipate will provide angular contrast. To produce the MCI, we first subtract the mean background (noisefloor) from the entire image. Sum projections in the A-line direction are then computed for the FI and HOI. MCI is generated as the pixel-wise division of the *en face* FI over the *en face* HOI.

Next, we generate MCI of an histopathology-confirmed adenocarcinoma within a sub-segmental airway (LB9b1). This image was selected from a previous OCT-AFI trial at the British Columbia Cancer Agency (BCCA) as it has good localization of a malignancy, as previously described in Pahlevaninezhad *et al.* Figure 2(e) [16]. Imaging of human subjects was approved by the Research Ethics Boards of the University of British Columbia and the British Columbia Cancer Agency (H14-00695). Patients were recruited from those referred to the BCCA for radial endobronchial ultrasound (R-EBUS) examination of CT-detected peripheral nodules. Informed written consent was obtained from all participants. Briefly, flexible bronchoscopy was conducted under local anesthesia and conscious sedation. Nodules were initially localized with R-EBUS, and then the ultrasound catheter was removed and replaced with the OCT-AFI catheter. As with the fingertip phantom, the noisefloor is subtracted from the image and *en face* sum projections are generated in the A-line direction to generate the FI and HOI which are then used to produce the MCI.

4. Results & discussion

4.1. FI and HOI modal characterization

An S^2 plot demonstrating the modes coupled across the FORJ and transmitted through a length of DCF as a function of effective refractive index is shown in Fig. 5(a). The plot shows a prominent excitation at DC corresponding to the LP_{01} mode (i), and a broad excitation occurring from $0.0030 < -\Delta n_{l,m} < 0.0055$ corresponding to LP_{11}-like modes (ii). In each excitation, the TMP remains confined to the geometric area of the DCF core (Fig. 5(a) i, ii insets). Note that the LP_{01} mode visible at DC corresponds to the FI, and the broad excitation region of LP_{11}-like modes corresponds to the blurred HOI which has previously been confirmed by comparing the effective index difference to the A-line delay between FI and HOI [27].

The modal wavelength dependence is further explored by generating a spectrogram (Fig. 5(b)). Here, the excitations for both the FI and HOI remain clearly visible and excited over all tested wavelengths 1266-1357 nm (not cut-off). This may seem unexpected: the core of this DCF is designed to be single-mode for wavelengths above 1250 nm, and so one might expect the HOMs to be cut-off in this spectral region. However, use of the term cut-off within a DCF core can be misleading. Within a SMF, for wavelengths above the cut-off of a mode, that mode is no longer guided through the fiber. Within a DCF, core modes at wavelengths above cut-off continue to propagate as inner-cladding modes. Moreover, for some inner-cladding HOMs (in

Optics EXPRESS

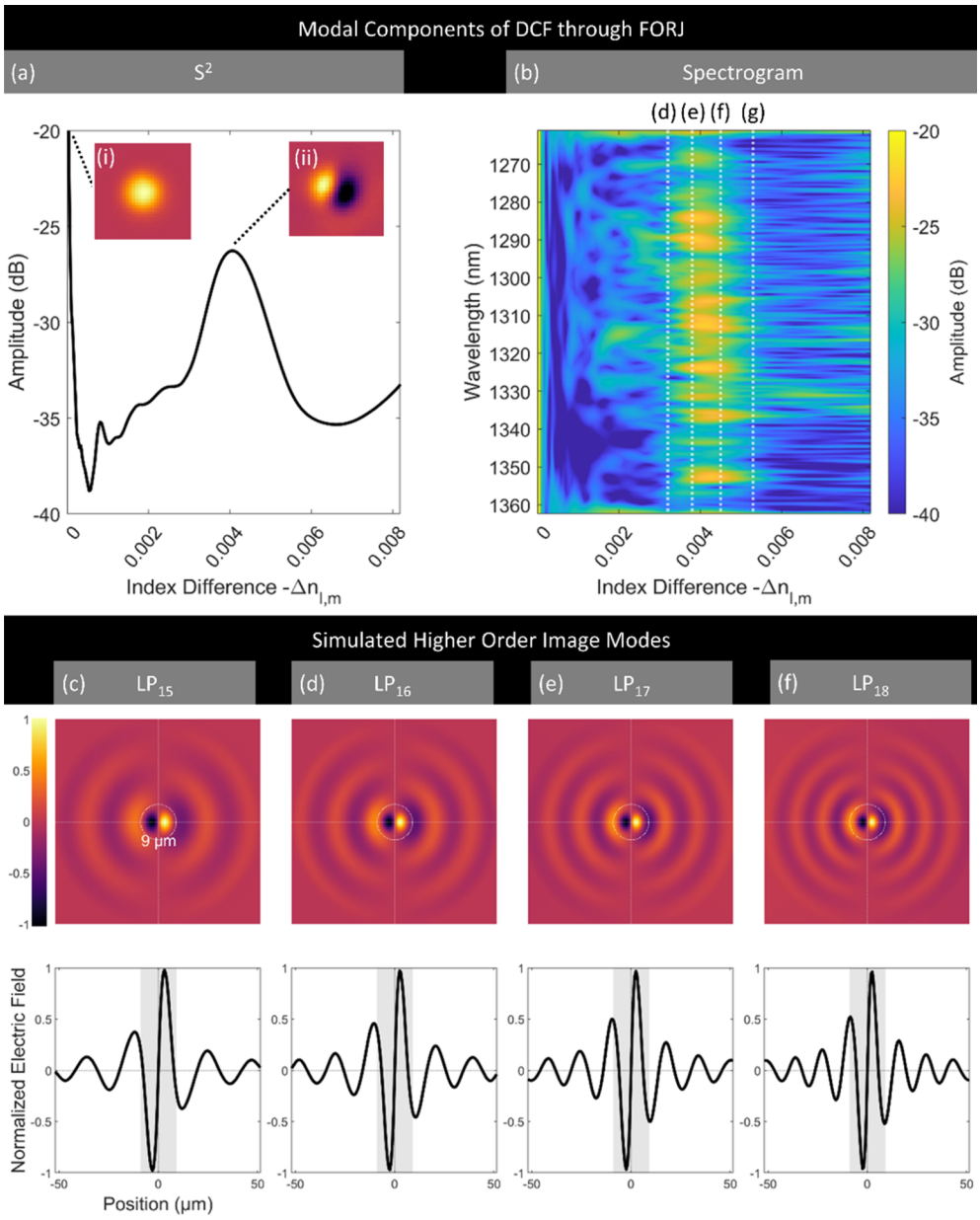

Fig. 5. (a) S^2 plot of the DCF through the FORJ. Insets demonstrate real space electric field plots scaled from [-1,1] of prominent modes: (i) the fundamental mode, (ii) the LP_{11}-like mode resulting in the HOI. (b) A spectrogram generated with the S^2 data. There is a prominent band at an index difference $-\Delta n_{l,m}$ of 0.003 to 0.0055 corresponding to the HOI. Dashed lines show the simulated effective refractive index of candidate inner-cladding modes for the HOI. (c) Real space electric field image and plot of the LP_{15} mode generated from simulation. (d) LP_{16} mode. (e) LP_{17} mode. (f) LP_{18} mode. We denote the geometric area of the core with a white circle in the radial illustration, and by a gray box in the cross-section.

Optics EXPRESS

particular LP_{1X} modes), the higher refractive index of the core causes strong excitations within the geometric area of the core [28].

These modes will also exhibit weaker excitations extending into the geometric area of the inner-cladding. However, these additional excitations are either obscured by interference with other inner-cladding modes with similar $\Delta n_{l,m}$ values or remain below the background levels of our measurement. This experiment made use of a custom tunable wavelength source and was performed in the presence of unavoidable mechanical vibrations. Adequately visualizing the fringes of the HOMs extending into the geometric area of the inner-cladding would likely require the S^2 imaging apparatus to be isolated from external disturbances. Thus, we predict the modal structure of the excitations by matching the measured $\Delta n_{l,m}$ values to modes generated from simulation. From this analysis, we postulate that the multipath artifact corresponds to a combination of the LP_{15}, LP_{16}, LP_{17}, and the LP_{18} modes; their $\Delta n_{l,m}$ values are indicated on Fig. 5(b) and their respective simulated TMPs are displayed in Fig. 5(c)-(f). We denote the geometric area of the core in each image using a white circle for the radial plot and a grey region within the modal cross-section.

In addition to determining the modal composition of the HOI, performing the S^2 imaging experiment through a FORJ allows for quantification of the cross-coupling efficiency $\beta_{l,m}$. This value will be encoded into the S^2 plot (Fig. 5(a)) as it visualizes the power coupled from a LP_{01} mode into the HOMs across the FORJ. We assume that the FORJ is a linear optical system and as such the measured cross-coupling between the LP_{01} mode into the inner-cladding modes will be equivalent to the cross-coupling from those same modes into the LP_{01} mode.

4.2. Differential coupling of Mie scatterers

Having identified and imaged the modes of the FI and HOI excited through a FORJ, we can quantify their coupling efficiencies for the backscattered electric fields of Mie scatterers. We illustrate the differential coupling into the FI (Fig. 6(a)) and HOI (Fig. 6(b)) by displaying the far-field profiles of the two excitations, their overlap for 10 and 15 μm microspheres (ii, iii), and a polar representation of the microsphere scattering phase function and TMP (iv, v).

The FI far-field mode profile is a Gaussian, predominantly capturing direct (low-angle) scattering. In contrast, the HOI far-field mode profile is a ring-like aperture; each TMP comprising this ring has an LP_{11}-like structure, however the lobes rotate azimuthally with effective refractive index through the HOI excitation.

The backscattering far-field profile of Mie scatterers appears as concentric rings analogous to an etalon interference pattern. The width, intensity and frequency of these rings are related to the wavelength of light and the size of the Mie scatterer; as the size of the scatterer increases, more intensity is carried at low backscattering angles.

Analyzing the overlap of the 10 and 15 μm scattering profiles with the modal excitations, there is a decrease in the power coupled into both the FI (Fig. 6(a). iii, v) and HOI (Fig. 6(b). iii, v) for the larger sphere. However, for the HOI excitation, the magnitude of decrease is larger. This is likely due to greater coupling between the 10 μm scatterer and the HOI due to the higher-angle backscattering fringes characteristic of smaller scatterers (Fig. 6(b). iv). Equivalently, the 15 μm scatterer has a more direct backscattering phase function, causing less coupling into the HOI (Fig. 6(a). v).

These observations are then quantified by plotting the mean coupling efficiencies of the FI and HOI as a function of microsphere diameter (Fig. 7(a)). Comparing the curves there is a visible difference between the coupling efficiencies, particularly for the smaller spheres ($< 12\,\mu m$). These differences are further demonstrated by plotting the ratio of the mean coupling efficiencies in Fig. 7(b). This measurement is analogous to the MC, defined by the ratio of the powers coupled into the FI and HOI. Analyzing this plot, a trend of increasing MC with microsphere

Optics EXPRESS

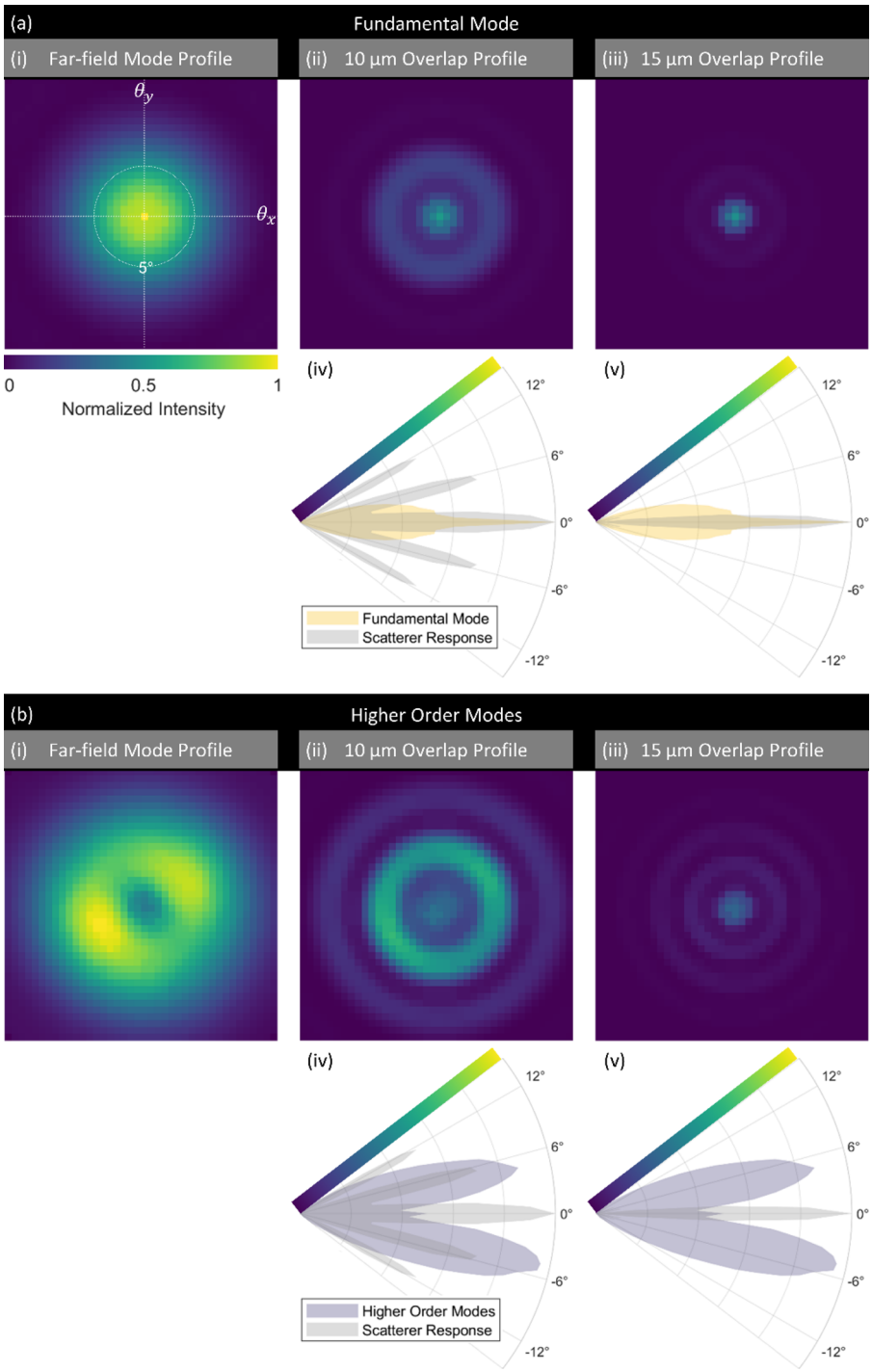

Fig. 6. Far-field modal footprints and coupling profiles of (a) the FI (LP_{01}) and (b) the HOI. (i) Far-field representation of the mode. (ii) Overlap between the scattering of a 10 µm sphere and their respective TMP. (iii) Overlap between the scattering of a 15 µm sphere and their respective TMP. (iv) Polar representation of the central row of the TMP ($\theta_y = 0$) and scattering phase function of a 10 µm sphere. (iv) Polar representation of the central row of the TMP ($\theta_y = 0$) and scattering phase function of a 15 µm sphere

Optics EXPRESS

size is apparent. This suggests that by quantifying the MC within OCT images, we could gain insight into sub-resolution tissue morphology.

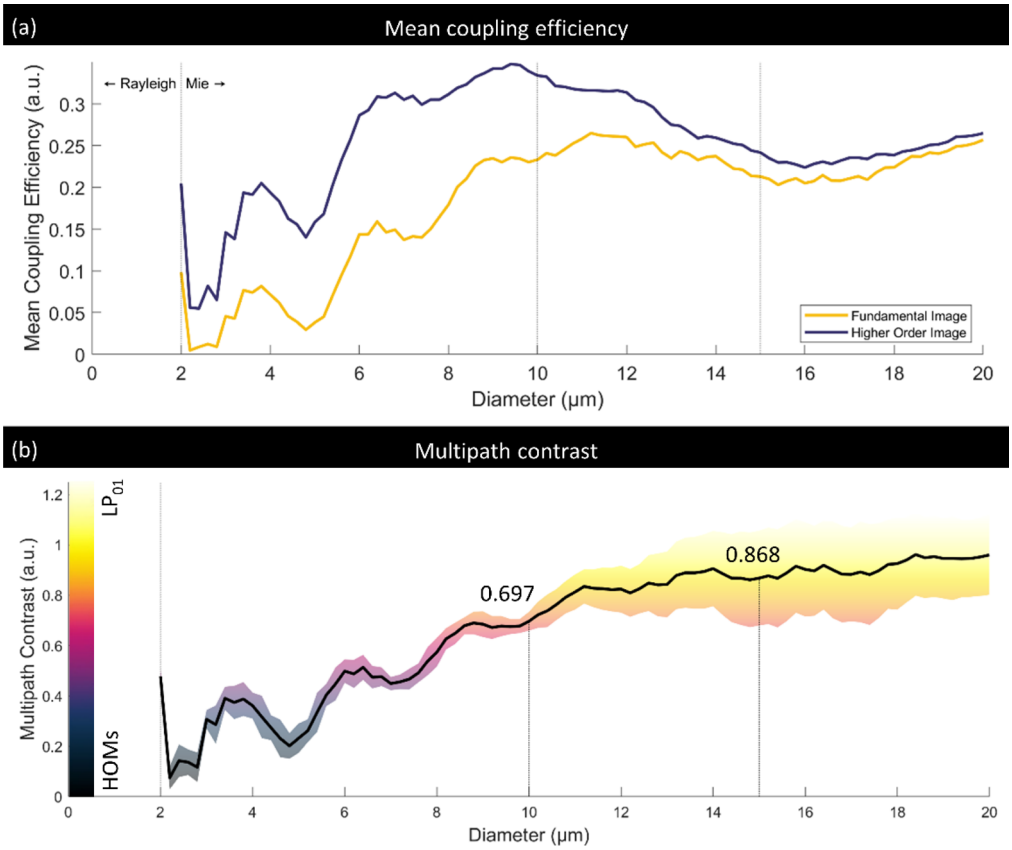

Fig. 7. Mean modal coupling and multipath contrast from simulated Mie scattering of polystyrene spheres immersed in water. Mie scattering model is valid for particles >2 µm (vertical dashed line) at 1310 nm. (a) Mean coupling efficiency for the FI (gold) and HOI (purple) as a function of scatterer diameter. (b) Multipath contrast calculated by dividing the coupling efficiency of the FI and HOI in (a). There is a trend of increasing MC with particle size; MC for 10 and 15 µm spheres are indicated. The translucent band represents the standard deviation of the curves over the wavelength band (1260-1360 nm).

4.3. Differential coupling in endoscopic OCT-AFI

The modeled MC values for polystyrene spheres can be compared to values generated from imaging. A sample OCT cross-section (B-frame) of the 15 µm diameter sphere dilution is shown in Fig. 8(a), with the FI appearing at the bottom of the image and the HOI at the top. As expected, the HOI of the sphere is blurred in the A-line direction resulting from the numerous inner-cladding modes. The sum of the intensities within the averaged FIs and HOIs can be used to calculate the MC for the 10 and 15 µm scatterers (Fig. 8(b) and 8(c) respectively). We calculate the MC for the 10 µm scatterers to be 0.680 for and 0.934 for 15 µm scatterers. Comparing these values to the modelled MC values in Fig. 7(b), we see that they follow the trend of increasing MC with particle diameter. Moreover, the values closely match those generated from the modes measured using S^2 (0.697 for 10 µm and 0.868 for 15 µm).

Optics EXPRESS

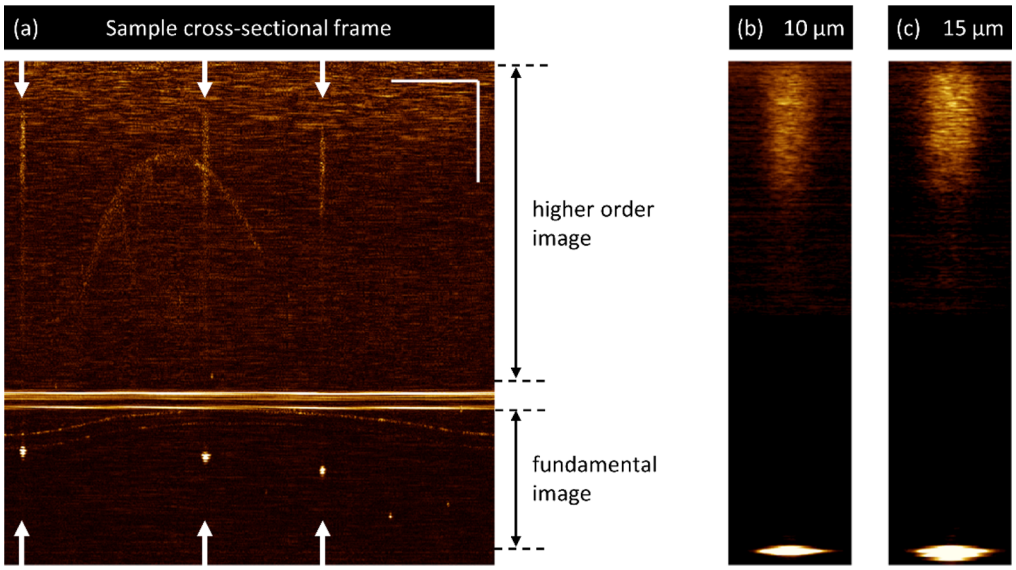

Fig. 8. (a) Sample cross-section of the 15 µm microsphere liquid dilution. Scale bars are 1 mm. Arrows indicate microspheres, and their trails in the HOI can be seen directly above their FI counterparts. 15 spheres were averaged out of the liquid microsphere phantom to generate point spread functions for the (b) 10 µm and (c) 15 µm microspheres. (b) and (c) are brightened and stretched horizontally to allow for the HOI to be visualized.

Despite this close match, we note that the values measured from these phantoms are not directly equivalent to those from the simple coupling model. OCT is acquired through an imaging catheter with a reflective element, a layer of Polyethylene terephthalate, and an outer sheath of Pebax 7433 (Rose Medical) between the sample and the focusing lens. These elements change the beam path, but also introduce additional reflections visible in both the FI and HOI. Due to the axial blurring of the HOI, these reflections are superimposed over the response of the microsphere, altering the total power within the HOI component of the MC. By averaging multiple microspheres (n = 15) from different depths in the A-line direction we mitigate this effect somewhat, but the impact of these packaging layers of the image catheter cannot be totally removed.

4.4. In vivo multipath contrast imaging

First, we present imaging of a human fingertip to illustrate MCI. For this image, the reference arm is set such that the FI and HOI do not overlap (visible in the longitudinal cross section in Fig. 9(a)). Within the *en face* of the FI (Fig. 9(b)), the ridges of the finger appear bright. Contrasting this, within the HOI *en face* (Fig. 9(c)), the creases appear brighter. These differences are better visualized by the MC image (Fig. 9(d)), where the low-angle scattering from the ridges of the fingers result in a relative increase in coupling into the fundamental mode, compared to the higher angled scattering from the creases which favor the HOMs.

This phantom also highlights a potential limitation of MCI: the angle at which the tissue is imaged will impact the MC response. A close look at the space between the two fingers shows that the sharp differentiation between the ridges and creases is lost. This effect is likely multi-factorial: the reflection from the surface of the tissue now couples into the fiber at angles greater than the undulations of the fingerprint, causing a relative increase in HOI coupling. Additionally, imaging the fingertip at an angle which is not orthogonal to the dermal-epidermal boundary means that we predominantly capture epidermis. This will change the MC of the sample given the difference in scattering between these layers.

Optics EXPRESS

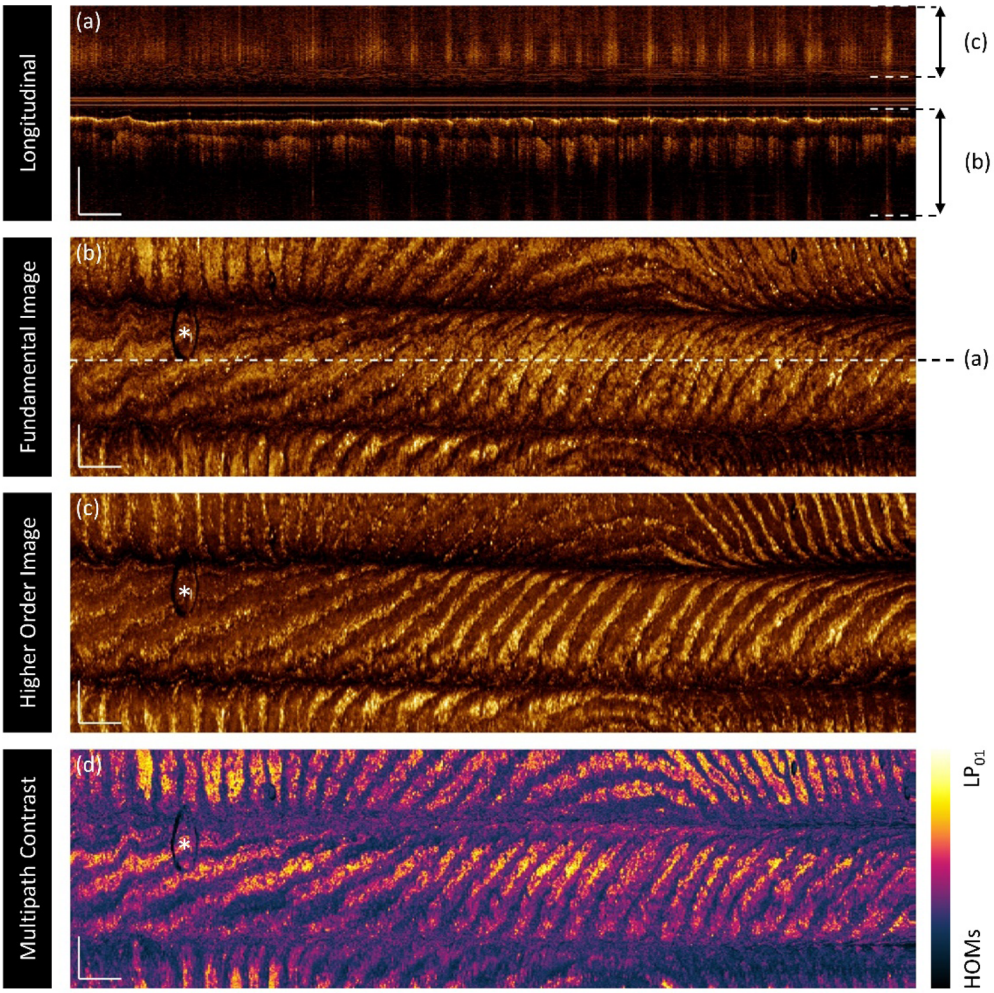

Fig. 9. OCT and multipath contrast of a human fingertip. Scale bars are 1 mm; an air bubble is indicated with an asterisk *. A longitudinal slice (a) is taken from the dashed line in panel (b). Panels (b-c) demonstrate *en face* views of the sample: (b) and (c) are sum projections taken of the FI and HOI regions respectively as indicated in panel (a). Panels (b) and (c) demonstrate different features – for instance, the narrow and dark grooves in the fingertip shown in the FI (b) appear as broad bright regions in the HOI (c). This is further illuminated in (d), a view generated by the pixel-wise division of (b) and (c) where bright yellows represent greater relative coupling into the FI while dark purples represent greater coupling into the HOI.

Optics EXPRESS

Next, we demonstrate MCI has potential to complement OCT-AFI in an adenocarcinoma acquired *in vivo* from a lung cancer patient (Fig. 10). The left-hand side of this image is distal (deeper into the subsegmental airway LB9b1) and the right-hand side is proximal (closer to the bronchoscope). Parenchymal structures such as alveolar texture, ducts, and vasculature are generally visualized in the more distal region of endobronchial OCT, whereas the proximal regions may have more smooth muscle or cartilage rings [44].

The suspected lesion is prominently visualized as the largest signal-poor area within the AFI (marked in Fig. 10(a)). Analyzing a longitudinal section in OCT (Fig. 10(b)) which bisects the low fluorescence area, a thickened epithelial layer is visualized. Within both the *en face* FI and HOI (Fig. 10(c) and 10(d) respectively) the suspected lesion is not easily distinguishable from the surrounding tissue beyond a loss of bright reflections from air-tissue gaps associated with alveoli and emphysema-like structures (highly reflective dots in both images). However, in MCI (Fig. 10(e)) there is a visible increase in response, suggesting that there is a decrease in backscattering angle over the lesion (circled) compared to the surrounding tissue. The higher MC in the lesion supports our modelling: carcinomas are characterized by an increase in both overall cell size and nuclear size within the Mie scattering range [41,45]. Despite this, we note that a more complex model accounting for multiple scattering, macroscopic tissue structures (alveoli), and stratified tissue layers is necessary to develop a robust model for carcinoma.

Additional to the increased MC over the lesion area, there is an increase at the left end of the image; similarly, a decrease in autofluorescence is seen over this region. From the OCT, the tissue is seen pulling away from the catheter and the residual gap is filled with mucus. This effect illustrates a limitation of AFI (or MCI) and a motivation for multimodal imaging. Co-registering these modalities with depth resolved imaging (OCT) allows for identification of such false positives. Despite the similar response between AFI and MCI for the lesion, different features are visible between the MCI and AFI. A diverse vascular network visible in the AFI (Fig.10a) is not visible in MCI (Fig. 10(e)). A close inspection of the bright reflections from sub-surface air-tissue gaps reveals that they appear more prominently in the HOI than the FI, thus appearing as dark speckles in MCI.

In addition to the differential features, we note a series of artifacts visible in the images. Prominent in the *en face* FI and the MCI are two dark bands running from left to right (* in Fig. 10(c) and 10(e)). These are known to result from interference variations associated with the rotating sample arm and stationary reference and can be corrected by implementing polarization diverse detection [46]. Of note, these bands are less prominent in the HOI, resulting in their appearance in MCI. We speculate that this is a result of the HOI being comprised of numerous HOMs with variable polarization states. Also visible in each image is a sharp discontinuity resulting from non-uniform rotational distortion (‡ in Fig. 10(a), and 10c-10e).

To our knowledge, there are no endoscopic multimodal OCT devices with a secondary modality that provides information regarding a backscattering angle of the sample. At a superficial level, trained clinicians could analyze MCI as a *heat-map*, identifying significant increases or decreases in the MC response. Analysis of co-registered OCT would then allow for identification of false-positives associated with a loss of tissue contact with the catheter. In this capacity MCI fills a similar role to AFI, though it interrogates different optical properties of the sample.

Before applying MC more broadly as a novel imaging modality in multimodal OCT systems, we must address the robustness and repeatability of this technique. First, there is the question of the stability of the HOI inner-cladding modes. Given that tissue scattering profiles are sampled at the end of the DCF image catheters, modal stability would not impact the profile coupled into the fiber. Rather, the mechanical manipulation of the imaging catheter would cause the modes to be scrambled and impact the cross-coupling through the FORJ. However, we previously quantified that the displacement of the FI and HOI is consistent with the specific inner-cladding modes displayed in Fig. 5 [27]. This relation holds true while imaging through a 1.65 m long

Optics EXPRESS

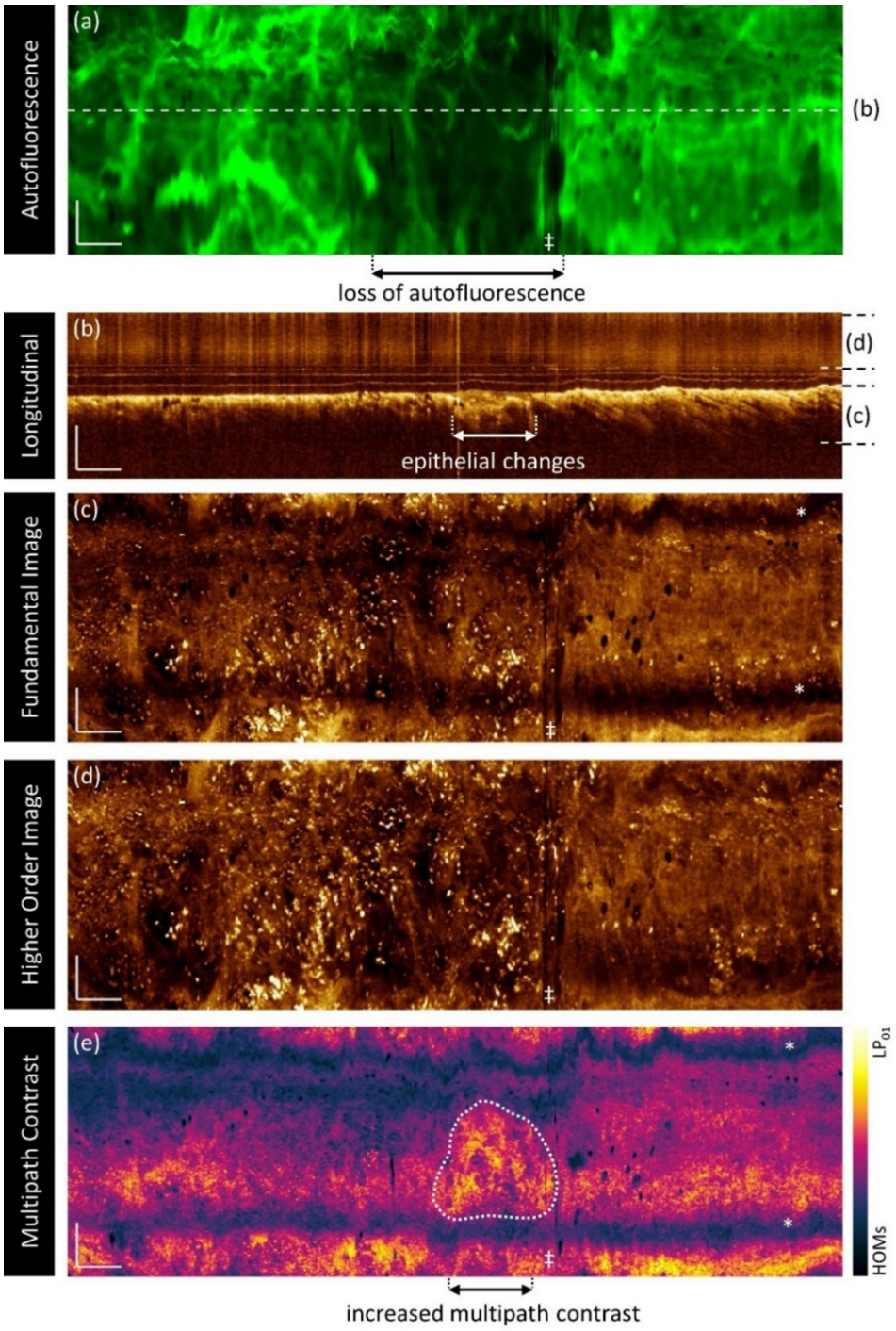

Fig. 10. OCT-AFI and multipath contrast of a sub-segmental airway (LB91b) in a human lung with a histology confirmed adenocarcinoma. Scale bars are 1 mm; * in (d) and (e) marks a banding artifact and ‡ marks a discontinuity from non-uniform rotational distortion. (a) AFI showing a decrease in autofluorescence over the area of the lesion. A longitudinal slice (b) is taken from the dashed line in panel (a), thickened epithelium corresponds to the lesion. (c) *En face* OCT projection over the FI region. (d) *En face* OCT over the HOI region. (e) Multipath contrast image revealing changes in the relative coupling into the FI and HOI between the lesion (circled) and surrounding tissue.

Optics EXPRESS

DCF imaging catheter, even while rapidly spinning and twisting the fiber proximally (up to 100 Hz frame rate). We suspect that modal instability would manifest as periodic changes in the coupling intensity and visible displacement of the HOI relative to the FI in the A-line direction resulting from a loss of power/modal cross-coupling between inner-cladding modes. However, as demonstrated within the *en face* projections of the HOI displayed in Fig. 8(c) and Fig. 9(d), we qualitatively observe no such effect.

We note that when implemented endoscopically, there is no control over the azimuthal directionality of the HOMs in this implementation. This is primarily due to the nature of endoscopic imaging with a relatively long (1.65 m) and high numerical aperture (DCF inner-cladding) fiber. The result is that the totality of the modes comprising the HOI resembles a ring in the far-field profile (Fig. 6(b). i) or near-field profile. This is reminiscent of annular structures used in darkfield imaging and illustrates the collection of higher-angle scattering into the HOI.

Beyond their stability, there are other considerations for why the same HOMs are consistently observed within the OCT interferogram. For the forward OCT imaging path, we note that HOMs would be excited (confirmed by the S^2 measurements displayed in Fig. 5) and would be incident upon tissue. Thus, light from these excitations will backscatter off the sample and could potentially result in a detected OCT signal. This could (1) resemble a further blurred HOI with an additional delay resulting from displacement along both the forward and return path, or (2) result in re-coupling of the HOMs into the fundamental mode along the return path that would superimpose the HOI. We have not observed the first phenomena and we speculate that the double-path modal dispersion and further attenuation through the FORJ results in the signal being below the noisefloor of our system. For the second phenomenon, the detected signal would be spatially aligned with the blurred HOI and we cannot at this time separate this from the mechanism described in section 2.

We see additional promise for this technique in inter-sample calibration of endoscopic OCT in clinical settings. There are many factors in clinical environments that result in changes in image quality between imaging sessions. Infection control requirements for *in vivo* imaging result in changes in the sample arm between imaging cases. Single-use image catheters may be required for high-risk sites (each image catheter with its own unique optical properties). In lower-risk sites, image catheters are detached between imaging cases for reprocessing, disinfection and/or sterilization. The result is that measured intensity of endoscopic OCT on different days is rarely comparable due to fluctuations in the laser power and frequent adjustments of the reference mirror. The ratiometric nature of MC measurements mitigates some of these effects. As in Eq. (8), the ratio of the total powers within the FI and HOI removes dependency on the reflectivity of the reference mirror (so long as it is set sufficiently well to resolve the images). However, we note that the coupling into the DCF modes is a function of the focusing optics and the cross-coupling through the joint responsible for MA generation (e.g., FORJ). The MC of images samples will be most comparable when the same imaging catheter and FORJ are used throughout a study.

5. Conclusion

This work demonstrates how multipath artifacts in DCF-based endoscopic OCT system may be leveraged to provide additional angular scattering information. Building upon previous work, we characterize the modes excited in a DCF catheter during endoscopic imaging (through a FORJ) and model the modal coupling efficiency for Mie scatterers of increasing size. Influenced by the results of this experiment, we propose multipath contrast imaging as a ratiometric visualization of the coupling in the fundamental mode over the higher-order modes to illustrate the angular diversity in a sample. We retrospectively generate MCI of a human fingertip and an *in vivo* adenocarcinoma in a subsegmental airway to demonstrate the application of this technique. We anticipate MCI can act as an adjunct to multimodal OCT, where the backscattering angle can aid in differentiating subtle structural changes that may not be visible by OCT. Multipath artifacts are

Optics EXPRESS

inherent to DCF-based OCT systems; thus, there is potential to retrospectively analyze previous clinical studies with MCI.

Funding. Natural Sciences and Engineering Research Council of Canada (RGPIN-2023-05592, RGPIN-2017-06685); Canadian Institutes of Health Research (CIHR FRN 151970).

Acknowledgments. We acknowledge support from Eric Brace, Chloe Hill, and Geoffrey Hohert. Data used in Figure 10 was collected by Drs. Hamid Pahlevaninezhad and Anthony Lee as part of a study in collaboration with Drs. Tawimas Shaipanich, and Stephen Lam.

Disclosures. The authors have no disclosures related to this work.

Data availability. Data underlying the results presented in this paper may be obtained from the authors upon reasonable request.

References

1. B. A. Flusberg, E. D. Cocker, W. Piyawattanametha, *et al.*, "Fiber-optic fluorescence imaging," Nat. Methods **2**(12), 941–950 (2005).
2. R. Cordova, K. Kiekens, S. Burrell, *et al.*, "Sub-millimeter endoscope demonstrates feasibility of in vivo reflectance imaging, fluorescence imaging, and cell collection in the fallopian tubes," J. Biomed. Opt. **26**(07), 076001 (2021).
3. J. M. Jabbour, M. A. Saldua, J. N. Bixler, *et al.*, "Confocal Endomicroscopy: Instrumentation and Medical Applications," Ann. Biomed. Eng. **40**(2), 378–397 (2012).
4. H. Pahlevaninezhad, A. M. D. Lee, T. Shaipanich, *et al.*, "A high-efficiency fiber-based imaging system for co-registered autofluorescence and optical coherence tomography," Biomed. Opt. Express **5**(9), 2978 (2014).
5. J. Mavadia, J. Xi, Y. Chen, *et al.*, "An all-fiber-optic endoscopy platform for simultaneous OCT and fluorescence imaging," Biomed. Opt. Express **3**(11), 2851 (2012).
6. S. Yuan, C. A. Roney, J. Wierwille, *et al.*, "Co-registered optical coherence tomography and fluorescence molecular imaging for simultaneous morphological and molecular imaging," Phys. Med. Biol. **55**(1), 191–206 (2010).
7. R. Guay-Lord, X. Attendu, K. L. Lurie, *et al.*, "Combined optical coherence tomography and hyperspectral imaging using a double-clad fiber coupler," J. Biomed. Opt. **21**(11), 116008 (2016).
8. K. Beaudette, J. Li, J. Lamarre, *et al.*, "Double-Clad Fiber-Based Multifunctional Biosensors and Multimodal Bioimaging Systems: Technology and Applications," Biosensors **12**(2), 90 (2022).
9. S. Liang, A. Saidi, J. Jing, *et al.*, "Intravascular atherosclerotic imaging with combined fluorescence and optical coherence tomography probe based on a double-clad fiber combiner," J. Biomed. Opt. **17**(7), 0705011 (2012).
10. L. Scolaro, D. Lorenser, W.-J. Madore, *et al.*, "Molecular imaging needles: dual-modality optical coherence tomography and fluorescence imaging of labeled antibodies deep in tissue," Biomed. Opt. Express **6**(5), 1767 (2015).
11. M. T. Tsai, C. H. Yang, S. C. Shen, *et al.*, "Noninvasive characterization of fractional photothermolysis induced by ablative and non-ablative lasers with optical coherence tomography," Laser Phys. **23**(7), 075604 (2013).
12. A. M. Fard, P. Vacas-Jacques, E. Hamidi, *et al.*, "Optical coherence tomography – near infrared spectroscopy system and catheter for intravascular imaging," Opt. Express **21**(25), 30849 (2013).
13. B. E. Sherlock, P. Vacas-Jacques, E. Hamidi, *et al.*, "Simultaneous, label-free, multispectral fluorescence lifetime imaging and optical coherence tomography using a double-clad fiber," Opt. Lett. **42**(19), 3753 (2017).
14. A. L. Buenconsejo, G. Hohert, M. Manning, *et al.*, "Submillimeter diameter rotary-pullback fiber-optic endoscope for narrowband red-green-blue reflectance, optical coherence tomography, and autofluorescence in vivo imaging," J. Biomed. Opt. **25**(03), 1 (2019).
15. X. Chen, W. Kim, M. Serafino, *et al.*, "Dual-modality optical coherence tomography and frequency-domain fluorescence lifetime imaging microscope system for intravascular imaging," J. Biomed. Opt. **25**(09), 096010 (2020).
16. H. Pahlevaninezhad, A. M. D. Lee, A. Ritchie, *et al.*, "Endoscopic Doppler optical coherence tomography and autofluorescence imaging of peripheral pulmonary nodules and vasculature," Biomed. Opt. Express **6**(10), 4191 (2015).
17. H. Pahlevaninezhad, A. M. D. Lee, G. Hohert, *et al.*, "Endoscopic high-resolution autofluorescence imaging and OCT of pulmonary vascular networks," Opt. Lett. **41**(14), 3209 (2016).
18. V. Backman, M. B. Wallace, L. T. Perelman, *et al.*, "Detection of preinvasive cancer cells," Nature **406**(6791), 35–36 (2000).
19. A. Wax, C. Yang, V. Backman, *et al.*, "Cellular Organization and Substructure Measured Using Angle-Resolved Low-Coherence Interferometry," Biophys. J. **82**(4), 2256–2264 (2002).
20. C. Compton, "Cancer Initiation, Promotion, and Progression and the Acquisition of Key Behavioral Traits," in *Cancer: The Enemy from Within: A Comprehensive Textbook of Cancer's Causes, Complexities and Consequences*, C. Compton, ed., (Springer International Publishing, Cham, 2020), pp. 25–48. doi: 10.1007/978-3-030-40651-6_2.
21. M. Monici, "Cell and tissue autofluorescence research and diagnostic applications," Biotechnol. Annu. Rev. **11**, 227–256 (2005).
22. J. Hung, S. Lam, J. C. LeRiche, *et al.*, "Autofluorescence of normal and malignant bronchial tissue," Lasers Surg. Med. **11**(2), 99–105 (1991).
23. J. A. Udovich, N. D. Kirkpatrick, A. Kano, *et al.*, "Spectral background and transmission characteristics of fiber optic imaging bundles," Appl. Opt. **47**(25), 4560–4568 (2008).

Optics EXPRESS

24. J. Li, S. Thiele, R. W. Kirk, *et al.*, "3D-Printed Micro Lens-in-Lens for In Vivo Multimodal Microendoscopy," Small **18**(17), 2107032 (2022).
25. F. Feroldi, M. Verlaan, H. Knaus, *et al.*, "High resolution combined molecular and structural optical imaging of colorectal cancer in a xenograft mouse model," Biomed. Opt. Express **9**(12), 6186 (2018).
26. K. Beaudette, H. Won Baac, W.-J. Madore, *et al.*, "Laser tissue coagulation and concurrent optical coherence tomography through a double-clad fiber coupler," Biomed. Opt. Express **6**(4), 1293 (2015).
27. A. Tanskanen, G. Hohert, A. Lee, *et al.*, "Higher-Order Core-Like Modes in Double-Clad Fiber Contribute to Multipath Artifacts in Optical Coherence Tomography," J. Lightwave Technol. **39**(17), 5573–5581 (2021).
28. A. Tanskanen, J. Malone, G. Hohert, *et al.*, "Triple-clad W-type fiber mitigates multipath artifacts in multimodal optical coherence tomography," Opt. Express **31**(3), 4465–4481 (2023).
29. P. Eugui, A. Lichtenegger, M. Augustin, *et al.*, "Beyond backscattering: Optical neuroimaging by BRAD," arXiv, arXiv:1712.00361 (2017).
30. P. Eugui, A. Lichtenegger, M. Augustin, *et al.*, "Few-mode fiber detection for tissue characterization in optical coherence tomography," presented at the *Optics InfoBase Conference Papers*, 2017. doi: .
31. P. Eugui, A. Lichtenegger, M. Augustin, *et al.*, "Simultaneous bright and dark field optical coherence tomography using few-mode fiber detection for neuropathology imaging," presented at the *Optics InfoBase Conference Papers*, 2018. doi: .
32. M. P. de Sivry-Houle, S. B. Beaudoin, S. Brais-Brunet, *et al.*, "All-fiber few-mode optical coherence tomography using a modally-specific photonic lantern," Biomed. Opt. Express **12**(9), 5704–5719 (2021).
33. J. A. Izatt and M. A. Choma, "Theory of Optical Coherence Tomography," in *Optical Coherence Tomography: Technology and Applications*, W. Drexler and J. G. Fujimoto, eds., (Springer International Publishing, Cham, 2015), pp. 65–94. doi: .
34. J. W. Nicholson, A. D. Yablon, S. Ramachandran, *et al.*, "Spatially and spectrally resolved imaging of modal content in large-mode-area fibers," Opt. Express **16**(10), 7233 (2008).
35. J. W. Nicholson, A. D. Yablon, J. M. Fini, *et al.*, "Measuring the modal content of large-mode-area fibers," IEEE J. Sel. Top. Quantum Electron. **15**(1), 61–70 (2009).
36. J. Jasapara and A. D. Yablon, "Spectrogram approach to S^2 fiber mode analysis to distinguish between dispersion and distributed scattering," Opt. Lett. **37**(18), 3906 (2012).
37. R. G. Stockwell, L. Mansinha, R. P. Lowe, *et al.*, "Localization of the complex spectrum: the S transform," IEEE Trans. Signal Process. **44**(4), 998–1001 (1996).
38. N. Sultanova, S. Kasarova, I. Nikolov, *et al.*, "Dispersion Properties of Optical Polymers," Acta Phys. Pol. A **116**(4), 585–587 (2009).
39. G. M. Hale and M. R. Querry, "Optical Constants of Water in the 200-nm to 200-µm Wavelength Region," Appl. Opt. **12**(3), 555–563 (1973).
40. J.-P. Schäfer, "Implementierung und Anwendung analytischer und numerischer Verfahren zur Lösung der Maxwell-gleichungen für die Untersuchung der Lichtausbreitung in biologischem Gewebe," Dissertation, Universität Ulm, 2011. doi: 10.18725/OPARU-1914.
41. Z. A. Steelman, W. J. Eldridge, J. B. Weintraub, *et al.*, "Is the nuclear refractive index lower than cytoplasm? Validation of phase measurements and implications for light scattering technologies," J. Biophotonics **10**(12), 1714–1722 (2017).
42. K.-B. Sung, R. Richards-Kortum, M. Follen, *et al.*, "Fiber optic confocal reflectance microscopy: a new real-time technique to view nuclear morphology in cervical squamous epithelium in vivo," Opt. Express **11**(24), 3171–3181 (2003).
43. J.-W. Su, W.-C. Hsu, C.-Y. Chou, *et al.*, "Digital holographic microtomography for high-resolution refractive index mapping of live cells," J. Biophotonics **6**(5), 416–424 (2013).
44. H. Long, J. Ji, L. Chen, *et al.*, "EB-OCT: a potential strategy on early diagnosis and treatment for lung cancer," Front. Oncol. **13**, 1156218 (2023).
45. I. Petersen, W. F. M. Amin Kotb, K.-H. Friedrich, *et al.*, "Core classification of lung cancer: Correlating nuclear size and mitoses with ploidy and clinicopathological parameters," Lung Cancer **65**(3), 312–318 (2009).
46. A. M. D. Lee, H. Pahlevaninezhad, V. X. D. Yang, *et al.*, "Fiber-optic polarization diversity detection for rotary probe optical coherence tomography," Opt. Lett. **39**(12), 3638–3641 (2014).